A comparative study on crystallization behavior, phase stability, and binding energy in pure and Cr-doped TiO_2 nanotubes

It Meng Low[a] and Hani Albetran
Department of Applied Physics, Centre for Materials Research, Curtin University, Perth, Western Australia 6845, Australia

Victor Manuel Prida and Victor Vega
Department of Physics, University of Oviedo, Calvo Sotelo s/n, 33007-Oviedo, Spain

Posman Manurung
Department of Physics, University of Lampung, Bandar Lampung 35145, Indonesia

Mihail Ionescu
Institute for Environmental Research, Australian Nuclear Science and Technology Organisation, Sydney, New South Wales 2234, Australia

(Received 7 May 2012; accepted 26 July 2012)

Use of nanostructured TiO_2 for photocatalysis is a cost-effective and sustainable technology. However, to make this an attractive viable technology will require the design of TiO_2 photocatalyst capable of harnessing the energy of visible light. One possible solution is the doping of TiO_2 to reduce its band gap. In this paper, the effect of Cr-doping by ion implantation on the in situ crystallization and phase stability of anodic TiO_2 nanotubes at elevated temperature is described. Cr-doping has dramatically reduced the fraction of anatase-to-rutile transformation and lowered the crystallization temperature of anatase from 600 to 400 °C and rutile from 600 to 500 °C. Ion beam analysis by Rutherford backscattering spectrometry has confirmed the existence of Cr ions composition gradation in doped TiO_2 nanotubes. The real doping of Ti lattices with Cr ions was evidenced by the analyses of surface compositions and chemical states of the nanotubes using x-ray photoelectron spectroscopy.

I. INTRODUCTION

Titanium dioxide (TiO_2) is a wide band gap semiconductor with energy of 3.0–3.2 eV. It is widely used in applications such as hydrogen production, gas sensors, photocatalytic activities, dye-sensitized solar cells, and photoelectrochemical cells because of its relative high efficiency and high stability.[1] However, due to its wide band gap energy, TiO_2 is active only under near-ultraviolet irradiation. Therefore, numerous studies have been carried out over the last 20 years to develop modified TiO_2 catalysts so that they are active under visible light irradiation (>400 nm). One of the most studied methods is by doping the TiO_2 materials with metal ions (Fe, Ni, Co, and Va)[2–5] or nonmetallic elements (N, S, and C).[6–15] For instance, N-doping of TiO_2 can result in visible light response by virtue of a narrowing in the band gap due to the mixing of *p* states of nitrogen with O 2*p* states. Among these doping methods, doping with transitional metals is one of the most efficient methods. Recent theoretical calculations showed that 3*d* transition metals such as Mn have good potential as a substitutional dopant for TiO_2 because of their ability to induce significant spin polarization and reduce the energy gap of rutile by forming intermediate bands with adequate curvatures and density of states.[16–18] Unlike defect states in the form of nearly straight horizontal lines within the energy gap, these curvy intermediate bands can act as stepping-stones to relay valence electrons to the conduction band.[16,17] As a result, the optical absorption edge of TiO_2 is shifted into the visible or even infrared spectral range of solar irradiance.[18]

Using a simple electrochemical anodization technique, highly ordered arrays of doped TiO_2 nanotubes with enhanced photocatalytic properties can be grown on a thin sheet of titanium.[19] X-ray photoelectron spectroscopy (XPS) results showed that the doped nanotube samples contained N, C, B, and F elements and the doped TiO_2 showed the shift in the band gap transition down to 2.98 eV. The photocatalytic activity of doped TiO_2 was 1.61 times better than undoped TiO_2.[15] Metals compounded on semiconductor materials increase charge collection efficiency due to a much slower electron–hole recombination, giving rise to longer electron lifetime, which will result in an increasing interfacial electron transfer process.[1,12]

Hitherto, the doping of TiO_2 has been widely synthesized using the sol–gel method.[20–24] However, ion implantation has now emerged as an alternative but effective doping method to improve the separation of the photogenerated

[a]Address all correspondence to this author.
e-mail: j.low@curtin.edu.au
DOI: 10.1557/jmr.2012.275

 © Materials Research Society 2012

https://doi.org/10.1557/jmr.2012.275 Published online by Cambridge University Press

electron–hole pairs or to extend the wave length range of the TiO_2 photoresponses into the visible region.[25–30] XPS measurements revealed that the implanted nitrogen species were mainly interstitial ones. The nitrogen concentration was increased with increasing the flux of ions, which could be controlled by adjusting the gas flow rate of the ion source, resulting in improved visible light photocatalytic activities.[26] Higher visible light photocatalytic efficiency was achieved with higher implanted nitrogen concentration.[26,27]

In this paper, we present x-ray diffraction (XRD) results on the role of Cr-doping on the in situ crystallization behavior and phase stability of TiO_2 nanotubes in the temperature range 25–1000 °C. The effect of Cr-doping on the resultant microstructure, composition depth profile, and binding energy is discussed in terms of scanning electron microscopy (SEM), ion beam analysis by Rutherford backscattering spectrometry (RBS), and XPS.

II. EXPERIMENTAL METHODS

A. Sample preparation

Ti foils (99.6% purity) with dimensions of $10 \times 10 \times 0.1$ mm^3 were used for the anodizing to produce self-organized and well-aligned TiO_2 nanotube arrays. The process of potentiostatic anodization was performed in a standard two-electrode electrochemical cell, with Ti as the working electrode and platinum as the counter electrode. Before anodization, Ti foils were mechanically polished, degreased by sonicating in ethanol, isopropanol, and acetone for 5 min each, followed by rinsing with deionized water, and then drying using nitrogen stream. After drying, the foils were exposed to the electrolyte, which consists of 100 mL of ethylene glycol, 2.04 mL of water, and 0.34 g of NH_4F. The electrolyte's pH was kept constant at pH = 6 and its temperature was kept at about 25 °C. The anodization process was performed under an applied voltage of 60 V for 0.5 h.[31,32] After that, the resulting TiO_2 structures were then rinsed in ethanol, immersed in hexamethyldililazane, and dried in air.

B. Cr-doping by ion implantation

The as-anodized samples were doped with Cr ions by exposure to a flux of ions directed perpendicular to the sample surface. The Cr ions were produced using a direct extraction high flux ion source, with a charge distribution close to the theoretical prediction (9% Cr^{+1}, 75% Cr^{+2}, 13% Cr^{+3}, 3% Cr^{+4}), corresponding to an average charge of +2.1, giving an average implantation energy of 63 keV. With these implantation parameters, the depth of Cr peak in TiO_2 is close to the stopping and range of ions in matter (SRIM) prediction of 35 nm. The near-surface composition depth profiling of ion-implanted samples was measured by RBS using He^{1+} ions at 1.8 MeV and the implanted dose was $\sim 7 \times 10^{14}$ ions/cm^2. This phase of work was conducted at the Australian Nuclear Science and Technology Organisation.

C. In situ high-temperature x-ray and synchrotron radiation diffraction

The in situ crystallization behavior of as-anodized or undoped TiO_2 was characterized using high-temperature XRD up to 1000 °C in air using an Anton Paar HTK16 hot stage (Graz, Austria). The XRD patterns were acquired in steps of 100 °C from 400 to 1000 °C. The mean crystallite sizes (L) of anatase and rutile were calculated from (101) and (110) reflections, respectively, using the Scherrer equation[33]:

$$L = \frac{K\lambda}{\beta \cos\theta} \quad , \tag{1}$$

where K is the shape factor (0.94), λ is the x-ray wave length, β is the line broadening at half the maximum intensity [full width at half maximum (FWHM)] in radians, and θ is the Bragg angle. The relative abundance of anatase and rutile at each temperature was computed using the Rietveld method. The models of Djerdj and Tonejc[34] and Howard et al.[35] were used to calculate the phase abundance of anatase and rutile, respectively, using the Rietica 1.7.7 software.

The in situ crystallization behavior of Cr-doped TiO_2 was characterized using high-temperature synchrotron radiation diffraction (SRD) up to 900 °C in argon to avoid oxidation of the implanted Cr ions. The SRD measurements were conducted at the Australian Synchrotron using the Powder Diffraction beamline in conjunction with an Anton Paar HTK20 furnace and the Mythen II microstrip detector. The SRD patterns were acquired in steps of 100 °C from 100 to 900 °C at an incident angle of 3° and wave length of 0.11267 nm.

The collected XRD and SRD data were analyzed using the CMPR program/software to evaluate the integrated peak intensities of all phases present. The sum of all the integrated peak intensities in 2θ range of 10°–50° was used to calculate the relative phase content of all the phases present at each temperature as follows:

$$W_A = \left(\frac{I_A}{I_A + I_R + I_T}\right) \times 100 \quad , \tag{2}$$

where W_A is the wt% of anatase, I_A is sum integrated intensity of anatase, I_R is sum integrated intensity of rutile, and I_T is sum integrated intensity of titanium. A similar ratio method was used to calculate the wt% of rutile (W_R) or titanium (W_T). This method is expected to be more accurate than the method of Spurr and Myers[36] where only the peak intensities of anatase (101) and rutile (110) are used. The use of integrated peak intensities in Eq. (2) can minimize issues relating to preferred orientation, grain

https://doi.org/10.1557/jmr.2012.275 Published online by Cambridge University Press

size, and/or degree of crystallinity. The CMPR program was also used to determine the FWHM of anatase (101) and rutile (110) reflections, respectively, to calculate the crystallite size using Eq. (1).

D. Scanning electron microscopy

The morphologies of the anodized and ion-implanted samples were characterized using a focused ion beam SEM operating at working distances of 5 mm with an accelerating voltage of 5 kV. The samples were gold-coated before the microstructure examination, and the images were taken using both secondary and backscattered electrons. Energy dispersive x-ray spectroscopy (EDS) was also conducted to analyze the elemental compositions of the samples.

E. X-ray photoelectron spectroscopy

XPS with Al K_α x-ray ($h\nu$ = 1486.6 eV) radiation operated at 150 W was used to investigate the surface properties and to obtain the valence band spectra. The operating pressure of the spectrometer was typically 1×10^{-9} Torr. The x-ray spot diameter was ~500 μm. The spectra were recorded in the fixed analyzer transmission mode with pass energy of 150 eV for recording survey spectra.

III. RESULTS AND DISCUSSION

A. Crystallization behavior

Figure 1 shows the XRD plots of undoped TiO_2 before and after thermal annealing in air at different temperatures ranging between 20 and 1000 °C. The anodic TiO_2 nanotube arrays before thermal treatment were amorphous but eventually crystallized at 400 °C to form anatase, which started to decrease in abundance but persisted at up to 1000 °C. A small amount of rutile started to form at 600 °C and its abundance increased rapidly after 800 °C, which corresponds to the rapid decrease in anatase. Since anatase is well known to be metastable, it began to transform into rutile at about 600 °C. Figure 2 shows that

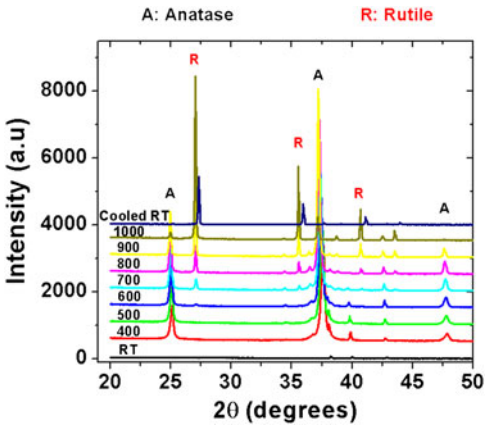


FIG. 1. High-temperature XRD plots for pure TiO_2 showing the in situ crystallization of anatase and rutile from the amorphous TiO_2 in the temperature range 20–1000 °C.

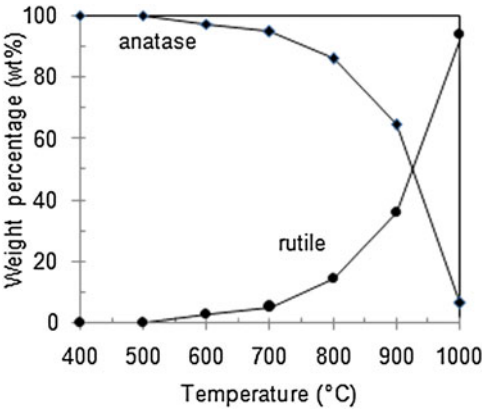


FIG. 2. Phase abundances of anatase and rutile for pure TiO_2 in the temperature range 20–1000 °C.

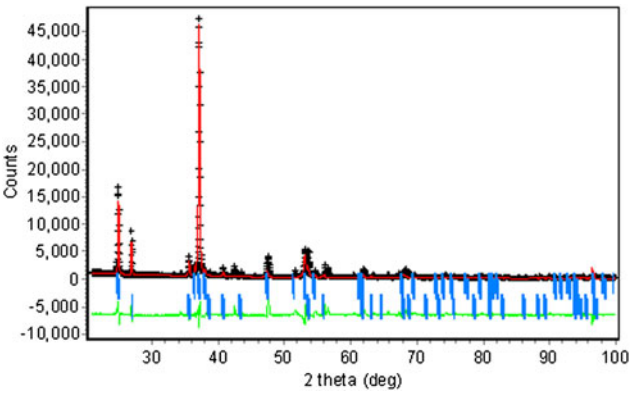


FIG. 3. XRD profile plot for pure TiO_2 nanotubes at 800 °C. Measured and calculated patterns are indicated by crosses (black) and solid line (red), respectively. Intensity differences between the two patterns are shown along the bottom of the plot (green). Vertical bars (blue) represent the allowable peak position for each of the phases (from top to bottom: anatase and rutile).

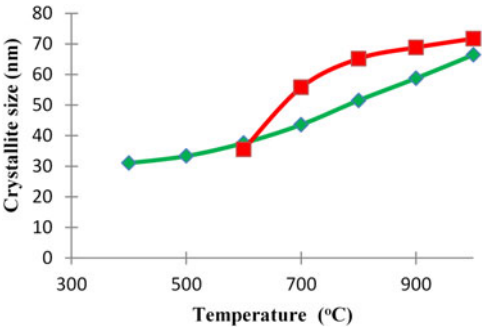


FIG. 4. Variations of crystallite size of anatase (♦) and rutile (■) as a function of temperature for pure TiO_2.

https://doi.org/10.1557/jmr.2012.275 Published online by Cambridge University Press

phase abundances of anatase and rutile as a function of temperature. A typical Rietveld profile fit for the XRD data at 800 °C is shown in Fig. 3. The good refinement quality of diffraction data can be discerned by the acceptable fitting parameters of $R_p = 17.4$; $R_{wp} = 26.0$; $R_{exp} = 3.5$; R_B (anatase) = 5; and R_B (rutile) = 10.

There was also a distinct narrowing and sharpening in the (101) peak for anatase and (110) peak for rutile. The corresponding increase in crystallite size calculated from the Scherrer equation is shown in Fig. 4. The crystallite size of anatase was about 30 nm at 400 °C and increased gradually with temperature to ~65 nm at 1000 °C. The crystallite size of rutile formed at 600 °C was about 35 nm, which grew rapidly and leveled off at 1000 °C with a size of 70 nm. It should be emphasized that the values of crystallite size reported here are only relative because the contribution of strains on peak broadening has been ignored in the calculation using the Scherrer equation.

The fraction of anatase-to-rutile transformation in the samples annealed at between 600 and 1000 °C can be calculated from the followed equation[36]:

TABLE I. Fractions of anatase-to-rutile transformation in pure and Cr-doped TiO_2 at various temperatures.

Temperature (°C)	x (%) TiO_2	x (%) Cr-doped TiO_2
500	...	0.6
600	4.4	3.6
700	16.4	4.6
800	30.3	5.6
900	59.6	...
1000	96.6	...

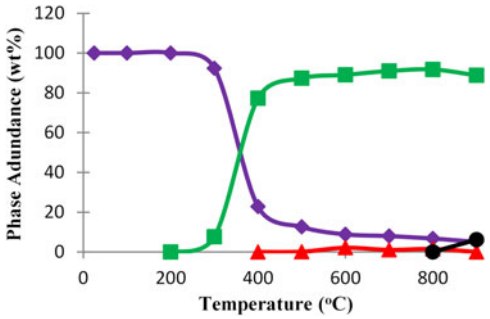


FIG. 6. Variations of phase abundances as a function of temperature for Cr-doped TiO_2 nanotubes. [Legend: titanium (♦); anatase (■); rutile (▲); TiO_{2-x} (●)].

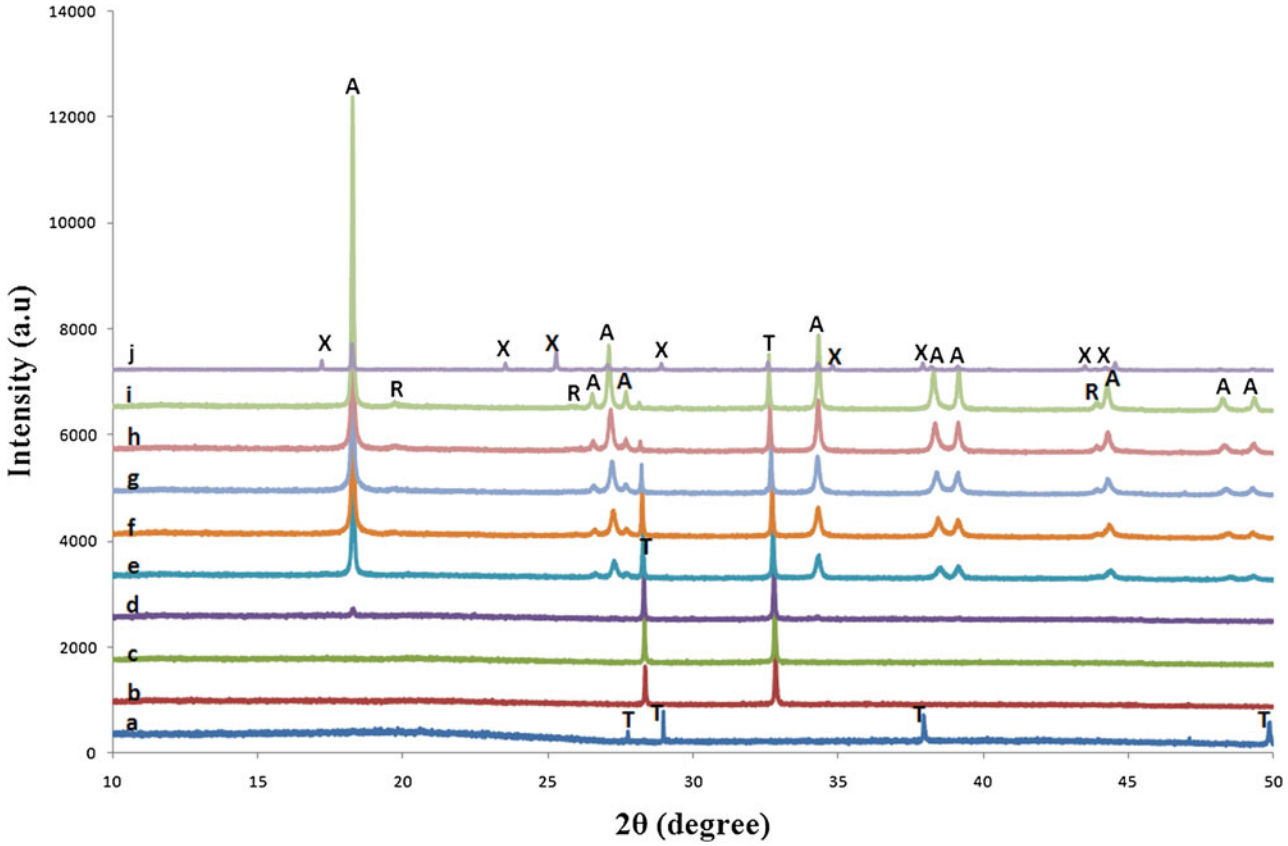


FIG. 5. In situ SRD plots of Cr-doped TiO_2 nanotubes showing the existence of anatase (A), rutile (R), Ti_5O_9 (X), and titanium (T) in the temperature range 20–900 °C. (Legend: a = 20 °C, b = 100 °C, c = 200 °C, d = 300 °C, e = 400 °C, f = 500 °C, g = 600 °C, h = 700 °C, i = 800 °C, j = 900 °C).

https://doi.org/10.1557/jmr.2012.275 Published online by Cambridge University Press

$$x = 1/[1 + 0.8(I_A/I_R)] \quad , \qquad (3)$$

where I_A is the x-ray integrated intensities of the (101) reflection of anatase at about 25.5°, while I_R is that of the (110) reflection of rutile at about 27.7°; x is the weight fraction of rutile in the nanotubes, which is calculated to be 4.4% for the nanotubes annealed at 600 °C, 16.4% at 700 °C, 30.3% at 800 °C, 59.6% at 900 °C, and 96.6% at 1000 °C (see Table I).

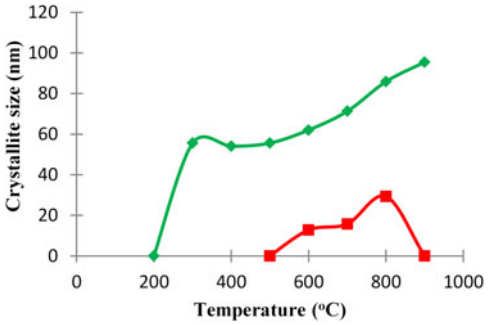


FIG. 7. Variations of crystallite size (L) of anatase (♦) and rutile (■) as a function of temperature for Cr-doped TiO_2 nanotubes.

Figure 5 shows the SRD plots of Cr-doped TiO_2 nanotubes before and after thermal annealing in argon at 20–900 °C. The TiO_2 nanotube arrays were initially amorphous but eventually crystallized to anatase at 300 °C. The peak intensities of anatase increased rapidly when the annealing temperature rises from 300 to 400 °C and continued to increase until 900 °C. The formation of rutile commenced at 500 °C but its growth was sluggish where the peak intensities increased very slightly from 500 to 800 °C. However, rutile disappeared at 900 °C with the concomitant appearance of TiO_{2-x} where $x = 0.2$ (see Fig. 6). This suggests that rutile was unstable in argon atmosphere at 900 °C and decomposed to form a non-stoichiometric titanium oxide and oxygen vacancies (O_v) as follows:

$$5TiO_2 \xrightarrow{900\,^{\circ}C/\text{argon}} Ti_5O_9 + O_v \quad . \qquad (4)$$

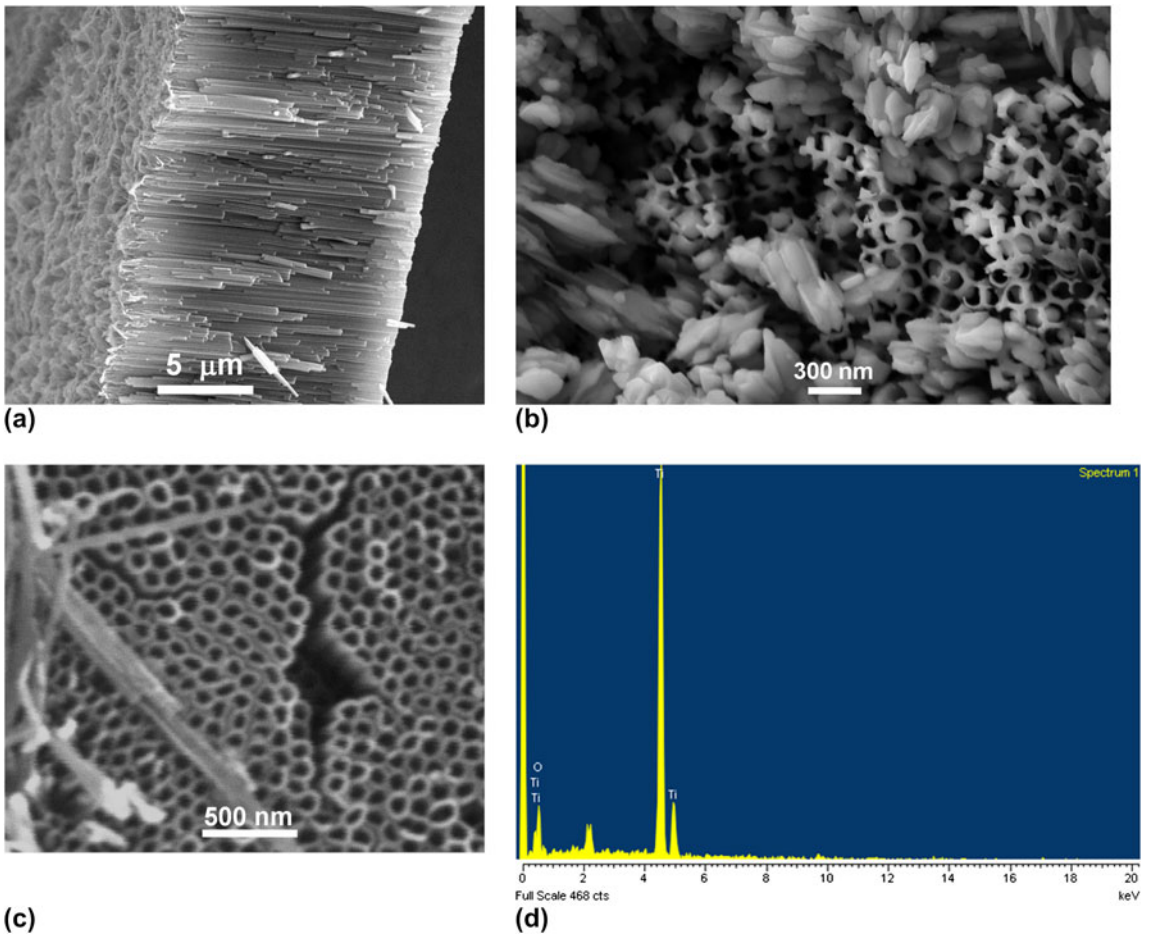


FIG. 8. Scanning electron micrographs showing the microstructure of pure TiO_2 nanotubes (a) at room temperature, (b) at 900 °C, (c) at 400 °C for 2 h, and (d) the corresponding EDS analysis of composition in Spectrum 1.

https://doi.org/10.1557/jmr.2012.275 Published online by Cambridge University Press

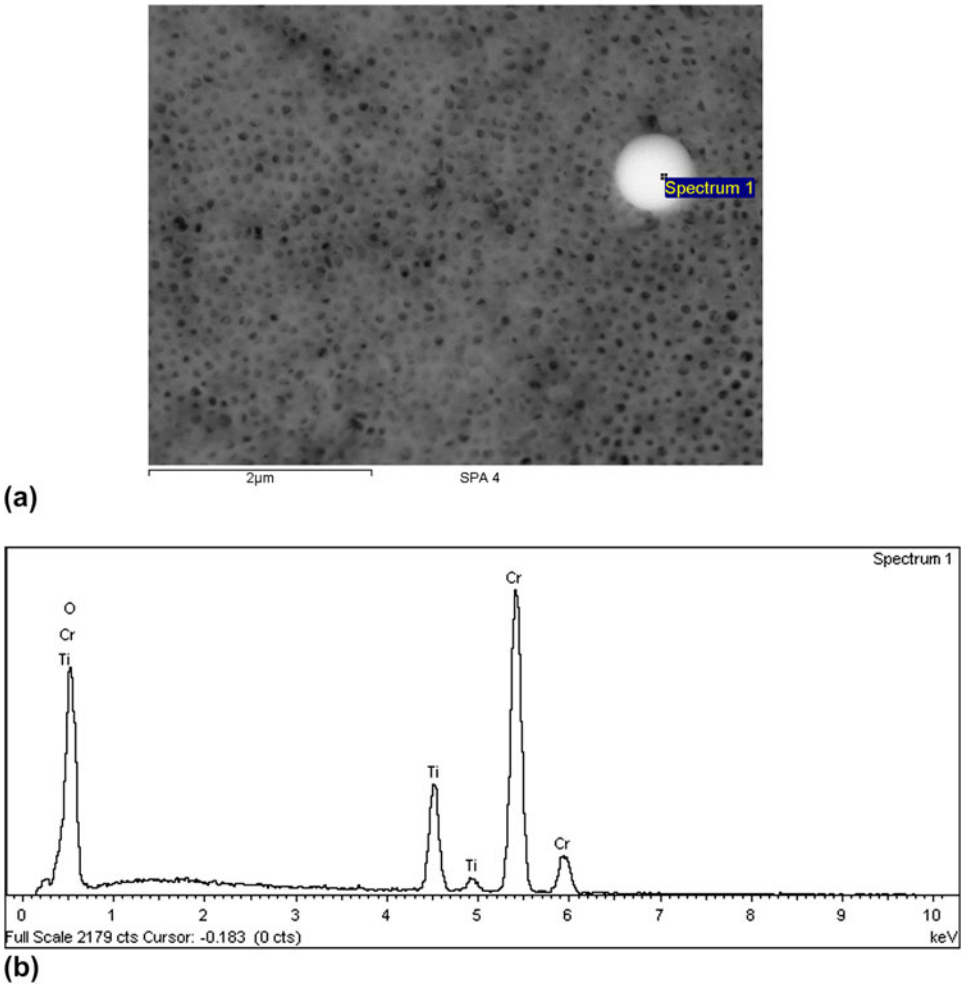


FIG. 9. Scanning electron micrographs showing the microstructure of (a) Cr-doped TiO_2, (b) EDS analysis of composition in Spectrum 1.

In contrast, no decomposition of rutile was observed in undoped TiO_2 nanotubes (see Fig. 1). When compared to Cr-doped TiO_2, both anatase and rutile in pure TiO_2 crystallized at a higher temperature, i.e., 400 and 600 °C, respectively. Using Eq. (3), the fraction of anatase-to-rutile transformation in Cr-doped TiO_2 at between 600 and 1000 °C was computed to be 0.6% at 500 °C, 3.6% at 600 °C, 4.6% at 700 °C, and 5.6% at 800 °C. As shown in Table I, these values are significantly when compared to pure TiO_2.

Figure 7 shows the influence of annealing temperature on crystallite size for anatase and rutile in Cr-doped TiO_2. The crystallite size of anatase was about 55 nm at 400 °C and increased gradually with temperature to 100 nm at 900 °C. In contrast, the crystallite size of rutile formed was much smaller than anatase and peaked at 700 °C with only 33 nm in size.

It appears that the presence of Cr-doping has accelerated the formation of anatase and rutile at a lower temperature, probably through the facilitation of defects such as vacancies. It is widely accepted that the onset temperature of the anatase to rutile phase transformation and the rate at which it proceeds can be affected significantly by dopants, firing atmosphere, microstructure, sample morphology, and the presence of impurities in the material.[1] The process of the anatase-to-rutile transformation is known to occur via (i) the nucleation of rutile at point defects, oxygen vacancies, secondary phase inclusions, particle surfaces, and/or at (112) twin interfaces in anatase and (ii) the subsequent consumption of the anatase phase by the growing rutile phase. The formation of rutile from the metastable phase anatase is reconstructive and so takes place through atomic rearrangement involving the breaking of two of the six Ti–O bonds in the TiO_6 octahedra.[37] As anatase transforms into rutile, significant grain growth takes place, resulting in lower surface area and thus poorer photocatalytic performance.

Transition metals (e.g., Cr) of variable valence are reported to enter the titania lattice and create oxygen vacancies through reduction effects as follows[1,38]:

https://doi.org/10.1557/jmr.2012.275 Published online by Cambridge University Press

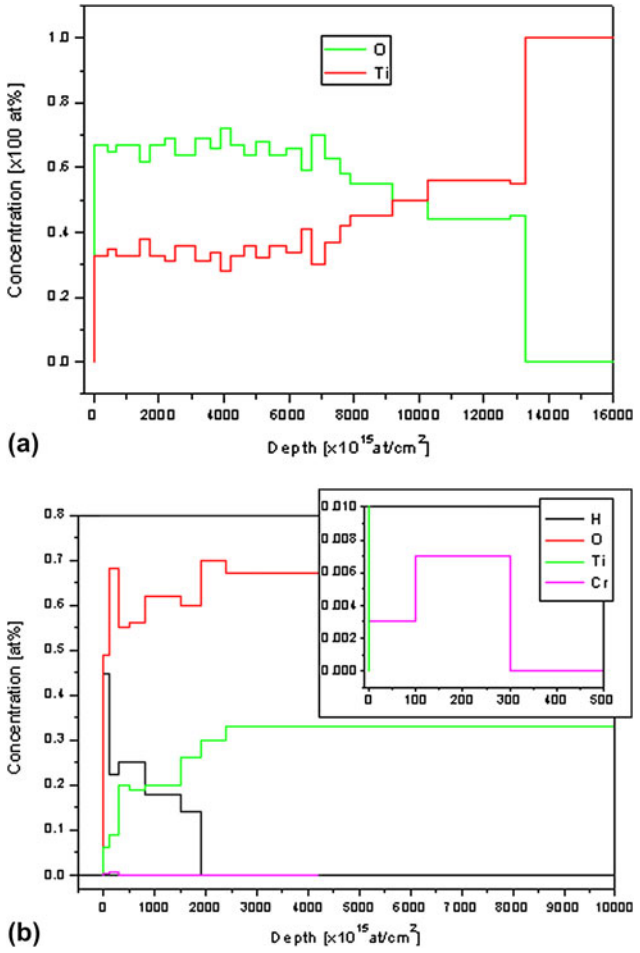


FIG. 10. Composition depth profiles in (a) pure TiO_2 and (b) Cr-doped TiO_2 nanotubes. Inset shows the close-up view of Cr concentration.

$$2M^{n+} + O^{2-} \rightarrow 2M^{(n-1)+} + \frac{1}{2}O_2 + O_v \quad , \qquad (5)$$

where M denotes a transition metal atom and O_v denotes an oxygen vacancy. Once substituted for Ti^{4+}, the reduction of such species gives rise to new oxygen vacancies and so enhances rutile formation from metastable anatase through easing of structural rearrangement. These oxygen vacancies are believed to be responsible for crystallization of anatase at a lower temperature in Cr-doped TiO_2 as well as destabilization and subsequent decomposition of rutile to form nonstoichiometric TiO_{2-x}.

B. Microstructures and formation mechanisms of nanostructured TiO_2

After anodizing in the electrolyte of NH_4F/H_2O/Ethylene glycol at 25 °C for 20 h, a homogeneous layer of TiO_2 nanotubes formed on the Ti foil. Figure 8(a) shows the SEM image of the microstructure of amorphous TiO_2 nanotubes in the as-anodized sample. Upon annealing at

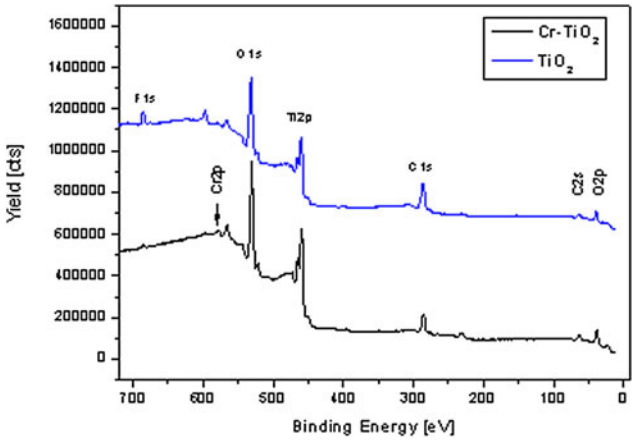


FIG. 11. XPS plots showing the chemical states and binding energies for pure and Cr-doped TiO_2 nanotubes.

400 °C for 2 h, vertically oriented and highly ordered arrays of anatase nanotubes with diameter of ~80 nm formed [Fig. 8(b)], which concur well with previous studies on anodized TiO_2.[39,40] The EDS analysis of nanotubes in Spectrum 1 of Fig. 8(c) indicated 31.04% Ti and 68.96% O, thus confirming the presence of TiO_2 in the sample. Upon annealing at 900 °C for 1 h, some anatase transformed into rutile that appeared as elongated grains randomly distributed among the nanotubes, as shown in Fig. 8(d).

The microstructure of Cr-doped TiO_2 is shown in Fig. 9(a) where the morphology of nanotubes has been retained during the process of ion implantation. The existence of implanted Cr ions has been verified by the EDS analysis of a bright region in Spectrum 1 as shown in Fig. 9(b).

C. Composition depth profiles and binding energies

The RBS results in Fig. 10 show the concentration of elements (at.%) versus depth (at./cm^2) for both the undoped and Cr-doped samples. The depth profile of Ti and O for undoped TiO_2 is shown in Fig. 10(a) where the composition at near-surface layer is fairly constant but a composition gradation in both O and Ti exists at the interface between the substrate and the oxide layer. In the Cr-doped sample [Fig. 10(b)], it is shown that a maximum Cr concentration of 0.7 at.% has been implanted in TiO_2 down to a depth of about 300 monolayers. A composition gradation also appears to exist at the interface between the substrate and the oxide layer.

The XPS plots in Fig. 11 show the binding energies of elements present in both undoped and Cr-doped TiO_2 nanotubes. The presence of Cr in the doped sample is evident by the display of Cr 2*p* peak. When compared to Cr-doped TiO_2, significantly, more fluorine is present in pure TiO_2. The cause of this diminished fluorine in Cr-doped TiO_2 is uncertain, although it is quite possible

https://doi.org/10.1557/jmr.2012.275 Published online by Cambridge University Press

that the process of ion implantation may have caused some fluorine to escape. Also noticeable is the slight peak shifts of Ti 2*p* and O 1*s* to the lower binding energy for Cr-doped TiO_2. Such peak shifts have also been observed for Cu-doped TiO_2.[41] This suggests that the Ti 2*p* binding energy in Cr-doped TiO_2 nanotubes increased when compared to that of pure TiO_2. The peak shift also illustrates the incorporation of Cr ions into the TiO_2 lattices. These results suggest that the Cr^{3+} ions are doped in the TiO_2 lattice forming a substitutional solid solution. When TiO_2 is doped with Cr^{3+} ions, the binding energy change in each atom occurs due to the electron transfer from Ti^{4+} to Cr^{3+}. In essence, the Fermi level of Cr_2O_3 is lower than that of TiO_2, thus resulting in the outer electron cloud density of Ti to decrease and that of Cr to increase.

IV. CONCLUSIONS

High-temperature SRD has been used to study the effect of Cr-doping on in situ crystallization of anatase and rutile in as-anodized TiO_2 nanotubes. The TiO_2 was initially amorphous but crystallized to anatase and rutile at elevated temperature. Cr-doping has lowered the crystallization temperature of anatase from 600 to 400 °C and rutile from 600 to 500 °C. In addition, it has reduced dramatically the fraction of anatase-to-rutile transformation. The rutile formed in TiO_2 was very stable after annealing at 1000 °C but became unstable in Cr-doped TiO_2, which decomposed to form TiO_{2-x} at 900 °C. Ion beam analysis by RBS has confirmed the existence of Cr ions composition gradation in doped TiO_2. The real doping of Ti lattices with Cr ions was evidenced by the analyses of surface compositions and chemical states of the nanotubes using XPS.

ACKNOWLEDGMENTS

This work was supported by funding from the Australian Synchrotron (PD-3611), the Australian Institute of Nuclear Science and Engineering (AINGRA-11134), and Spanish MAT2010-20798-C05-04. We thank Ms. E. Miller of Curtin Centre for Materials Research for assistance with the SEM work. The scientific support from the University of Oviedo SCTs, particularly to the Nanoporous Membranes Unit and Photo-electronic Spectroscopy Laboratories is also acknowledged.

REFERENCES

1. D. Hanaor and C. Sorrell: Review of the anatase to rutile phase transformation. *J. Mater. Sci.* **46**, 855–874 (2011).
2. M. Anpo, Y. Ichihashi, M. Takeuchi, and H. Yamashita: Design of unique titanium oxide photocatalysts by an advanced metal ion-implantation method and photocatalytic reactions under visible light irradiation. *Res. Chem. Intermed.* **24**, 143 (1998).
3. A. Zaleska, J.W. Sobczak, E. Grabowska, and J. Hupka: Preparation and photocatalytic activity of boron-modified TiO_2 under UV and visible light. *Appl. Catal., B* **78**, 92 (2008).
4. G.B. Saupe, T.U. Zhao, J. Bang, N.R. Desu, G.A. Carballo, R. Ordonem, and T. Bubphamala: Evaluation of a new porous titanium-niobium mixed oxide for photocatalytic water decontamination. *Microchem. J.* **81**, 156 (2005).
5. D.B. Hamal and K.J. Klabunde: Synthesis, characterization, and visible light activity of new nanoparticle photocatalysts based on silver, carbon, and sulfur-doped TiO_2. *J. Colloid Interface Sci.* **311**, 514 (2007).
6. J. Virkutyte, B. Baruwati, and R.S. Varma: Visible light induced photobleaching of methylene blue over melamine-doped TiO_2 nanocatalyst. *Nanoscale* **2**, 1109 (2010).
7. T. Umebayashi, T. Yamaki, and S. Tanaka: Visible light-induced degradation of methylene blue on S-doped TiO_2. *Chem. Lett.* **32**, 330 (2003).
8. S. Sakthivel, M. Janczarek, and H. Kisck: Visible light activity and photo-electrochemical properties of nitrogen-doped TiO_2. *J. Phys. Chem. B* **108**, 19384 (2004).
9. Y. Choi, T. Umebayashi, and M. Yoshikawa: Fabrication and characterization of C-doped anatase TiO_2 photocatalysts. *J. Mater. Sci.* **39**, 1837 (2004).
10. H. Irie, Y. Watanabe, and K. Hashimoto: Carbon-doped anatase TiO_2 powders as a visible-light sensitive photocatalyst. *Chem. Lett.* **32**, 772 (2003).
11. S. Sakthivel and H. Kisch: Daylight photocatalysts by carbon-modified titanium dioxide. *Angew. Chem. Int. Ed.* **42**, 4908 (2003).
12. R. Asahi, T. Morikawa, and T. Ohwaki: Visible-light photocatalysis in nitrogen-doped titanium oxides. *Science* **293**, 269 (2001).
13. W. Ren, Z. Ai, F. Jia, L. Zhang, X. Fan, and Z. Zou: Low temperature preparation and visible light photocatalytic activity of mesoporous carbon-doped crystalline TiO_2. *Appl. Catal., B* **69**, 138 (2007).
14. T. Ohno, M. Akiyoshi, T. Umebayashi, K. Asai, T. Mitsui, and M. Matsumura: Preparation of S-doped TiO_2 photocatalysts and their photocatalytic activities under visible light. *Appl. Catal., A* **265**, 115 (2004).
15. B.C. Bai, J.S. Im, J.G. Kim, and Y.S. Lee: Photo-catalytic degradation on B, C, N, and F element co-doped TiO_2 under visible-light irradiation. *J. Korean Ind. Eng. Chem.* **21**, 29–33 (2010).
16. G. Shao: Red shift in manganese- and iron-doped TiO_2: A DFT+U analysis. *J. Phys. Chem. C* **113**, 6800 (2009).
17. G. Shao: Electronic structures of manganese-doped rutile TiO_2 from first principles. *J. Phys. Chem. C* **112**, 18677 (2008).
18. X.H. Xia, L. Lu, A.S. Walton, M. Ward, X.P. Han, R. Brydson, J.K. Luo, and G. Shao: Origin of significant visible-light absorption properties of Mn-doped TiO_2 thin films. *Acta Mater.* **60**, 1974–1985 (2012).
19. P. Roy, S. Berger, and P. Schmuki: TiO_2 nanotubes: Synthesis and applications. *Angew. Chem. Int. Ed.* **50**, 2904–2939 (2011).
20. Y. Kuroda, T. Mori, K. Yagi, N. Makihata, Y. Kawahara, M. Nagao, and S. Kittaka: Preparation of visible-light-responsive $TiO_{2-x}N_x$ photocatalyst by a sol-gel method: Analysis of the active center on TiO_2 that reacts with NH_3. *Langmuir* **21**, 8026 (2005).
21. A. Hattori, M. Yamamoto, H. Tada, and S. Ito: A promoting effect of NH_4F addition on the photocatalytic activity of sol-gel TiO_2 films. *Chem. Lett.* **27**, 707 (1998).
22. Y. Shen, T. Xiong, T. Li, and K. Yang: Tungsten and nitrogen co-doped TiO_2 nano-powders with strong visible light response. *Appl. Catal., B* **83**, 177 (2008).
23. T.C. Jagadale, S.P. Takale, R.S. Sonawane, H.M. Joshi, S.I. Patil, B.B. Kale, and S.B. Ogale: N-doped TiO_2 nanoparticle based visible light photocatalyst by modified peroxide sol-gel method. *J. Phys. Chem. C* **112**, 14595 (2008).

https://doi.org/10.1557/jmr.2012.275 Published online by Cambridge University Press

24. Y. Tseng, C. Kuo, C. Huang, Y. Li, P. Chou, C. Cheng, and M. Wong: Visible-light-responsive nano-TiO_2 with mixed crystal lattice and its photocatalytic activity. *Nanotechnology* **17**, 2490 (2006).
25. T. Yamaki, T. Sumita, and S. Yamamoto: Formation of $TiO_{2-x}F_x$ compounds in fluorine-implanted TiO_2. *J. Mater. Sci. Lett.* **21**, 33 (2002).
26. H. Shen, L. Mi, P. Xu, W. Shen, and P.N. Wang: Visible-light photocatalysis of nitrogen-doped TiO_2 nanoparticulate films prepared by low-energy ion implantation. *Appl. Surf. Sci.* **253**, 7024 (2007).
27. J. Park, J.Y. Lee, and J.H. Cho: Ultraviolet-visible absorption spectra of N-doped TiO_2 film deposited on sapphire. *J. Appl. Phys.* **100**, 113534 (2006).
28. H. Yamashita, Y. Ichihashi, and M. Takeuchi: Characterization of metal ion-implanted titanium oxide photocatalysts operating under visible light irradiation. *J. Synchrotron Radiat.* **6**, 451 (1999).
29. T. Yamaki, T. Umebayashi, and T. Sumita: Fluorine-doping in titanium dioxide by ion implantation technique. *Nucl. Instrum. Methods Phys. Res., Sect. B* **206**, 254 (2003).
30. H. Yamashita, M. Harada, J. Misaka, M. Takeushi, and M. Anpo: Degradation of propanol diluted in water under visible light irradiation using metal ion-implanted titanium dioxide photocatalysts. *J. Photochem. Photobiol., A* **148**, 257 (2002).
31. V. Vega, V.M. Prida, M. Hernández-Vélez, E. Manova, P. Aranda, E. Ruiz-Hitzky, and M. Vázquez: Influence of anodic conditions on self-ordered growth of highly aligned titanium oxide nanopores. *Nanoscale Res. Lett.* **2**, 355 (2007).
32. V. Vega, M.A. Cerdeira, V.M. Prida, D. Alberts, N. Bordel, R. Pereiro, F. Mera, S. García, M. Hernández-Vélez, and M. Vázquez: Electrolyte influence on the anodic synthesis of TiO_2 nanotube arrays. *J. Non-Cryst. Solids* **354** 5233–5235 (2008).
33. B.D. Cullity and S.R. Stock: *Elements of X-Ray Diffraction*, 3rd ed. (Prentice-Hall Inc., Englewood Cliffs, NJ, 2001); pp. 167–171.
34. I. Djerdj and A.M. Tonejc: Structural investigations of nanocrystalline TiO_2 samples. *J. Alloys Compd.* **413**, 159–174 (2006).
35. C.J. Howard, T.M. Sabine, and F. Dickson: Structural and thermal parameters for rutile and anatase. *Acta Crystallogr., Sect. B: Struct. Sci* **47**, 462–468 (1991).
36. R.A. Spurr and H. Myers: Quantitative analysis of anatase-rutile mixtures with an x-ray diffractometer. *Anal. Chem.* **29**, 760 (1957).
37. S. Riyas, G. Krishnan, and P.N. Mohandas: Anatase-rutile transformation in doped titania under argon and hydrogen atmospheres. *Adv. Appl. Ceram.* **106**, 255 (2007).
38. K.J.D. Mackenzie: Calcination of titania V. Kinetics and mechanism of the anatase-rutile transformation in the presence of additives. *Trans. J. Br. Ceram. Soc.* **74**, 77 (1975).
39. V.M. Prida, M. Hernandez-Velez, K.R Pirota, A. Menendez, and M. Vazquez: Synthesis and magnetic properties of Ni nanocylinders in self-aligned and randomly disordered grown titania nanotubes. *Nanotechnology* **16**, 2696–2702 (2005).
40. O.K. Varghese, D. Gong, M. Paulose, C.A. Grimes, and E.C. Dickeya: Crystallization and high-temperature structural stability of TiO_2 nanotube arrays. *J. Mater. Res.* **18**, 156–165 (2003).
41. M. You, T.G. Kim, and Y.M. Sung: Synthesis of Cu-doped TiO_2 nanorods with various aspect ratios and dopant concentrations. *Cryst. Growth Des.* **10**, 983–987 (2010).

https://doi.org/10.1557/jmr.2012.275 Published online by Cambridge University Press